HHS Public Access

Author manuscript

NMR Biomed. Author manuscript; available in PMC 2023 March 01.

Published in final edited form as:

NMR Biomed. 2022 March ; 35(3): e4649. doi:10.1002/nbm.4649.

Dynamic contrast-enhanced CEST MRI using a low molecular weight dextran

Zheng Han[1,2,†], **Chuheng Chen**[3,†], **Xiang Xu**[1,2], **Renyuan Bai**[4], **Verena Staedtke**[4], **Jianpan Huang**[5], **Kannie W.Y. Chan**[1,5], **Jiadi Xu**[1,2], **David O. Kamson**[6], **Zhibo Wen**[7], **Linda Knutsson**[1,8], **Peter C.M. van Zijl**[1,2], **Guanshu Liu**[1,2,*]

[1]Department of Radiology, Johns Hopkins University, Baltimore, MD, USA

[2]F.M. Kirby Research Center for Functional Brain Imaging, Kennedy Krieger Institute, Baltimore, MD, USA

[3]Department of Biomedical Engineering, Case Western Reserve University, Cleveland, USA

[4]Department of Neurology and Neurosurgery, Johns Hopkins University, Baltimore, MD, USA

[5]Department of Biomedical Engineering, City University of Hong Kong, Hong Kong, China.

[6]The Sidney Kimmel Comprehensive Cancer Center at Johns Hopkins University, Baltimore, MD, USA.

[7]Department of Radiology, Zhujiang Hospital, Southern Medical University, Guangzhou, Guangdong, China

[8]Department of Medical Radiation Physics, Lund University, Lund, Sweden

Abstract

Natural and synthetic sugars have great potential for developing highly biocompatible and translatable Chemical Exchange Saturation Transfer (CEST) MRI contrast agents. In this study, we aimed to develop the smallest clinically available form of dextran, Dex1 (MW~ 1kDa), as a new CEST agent. We first characterized the CEST properties of Dex1 *in vitro* at 11.7T and showed the Dex1 had a detectable CEST signal at ~1.2 ppm, attributed to hydroxyl protons. *In vivo* CEST MRI studies were then carried out on C57BL6 mice bearing orthotopic GL261 brain tumors (n=5) using a Bruker Biospec 11.7 T MRI scanner. Both steady state full Z-spectral images and a single offset (1.2 ppm) dynamic dextran-enhanced (DDE) images were acquired before and after the intravenous injection of Dex1 (2 g/kg). The steady state Z-spectral analysis showed a significantly higher CEST contrast enhancement in the tumor than contralateral brain ($\Delta MTR_{asym}^{1.2\ ppm}$=0.010±0.006 vs. 0.002±0.008, P=0.0069) at 20 minutes after the injection of Dex1. Pharmacokinetic analyses of DDE were performed using area under the curve (AUC) in the first 10 minutes after Dex1 injection, revealing a significantly higher uptake of Dex1 in the tumor than brain tissue in tumor-bearing mice (AUC(0–10min) = 21.9±4.2 vs. 5.3±6.4 %·min, P=0.0294). In contrast, no Dex1 uptake was found in the brains of non-tumor bearing mice

*Corresponding author: Guanshu Liu, Ph.D., 707 N. Broadway, Baltimore, MD 21205, Phone (office): 443-923-9500; Fax: 410-614-3147, guanshu@mri.jhu.edu.

†:These authors contributed equally to this work

(AUC(0–10min) = −1.59 ± 2.43 %·min). Importantly, the CEST MRI findings were consistent with the measurements obtained by DCE MRI and fluorescence microscopy, demonstrating the potential of Dex1 as a highly translatable CEST MRI contrast agent for assessing tumor hemodynamics.

Graphical Abstract

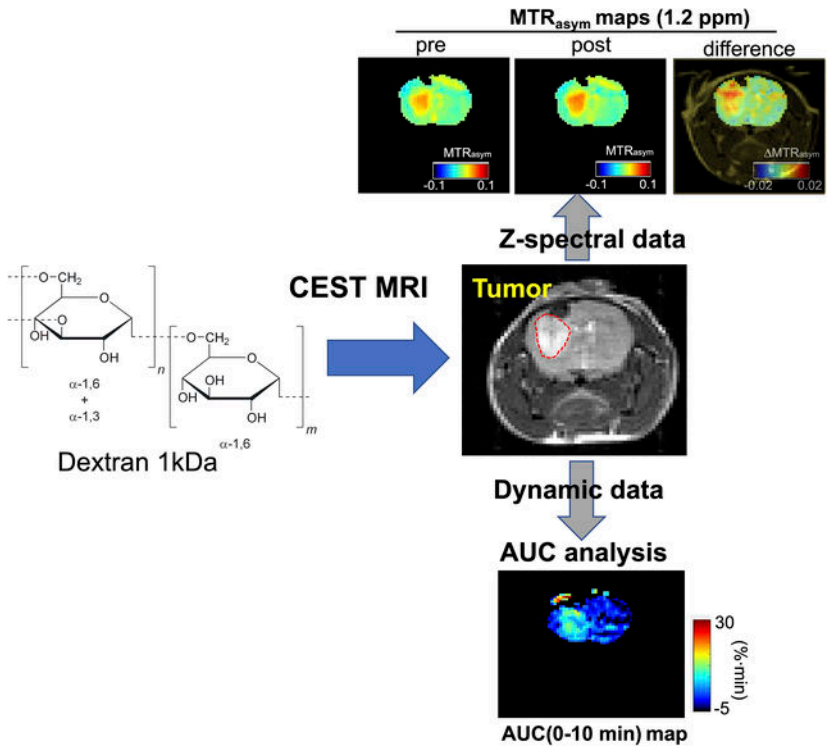

Keywords

CEST; MRI; dextran; brain tumor; permeability

Introduction

Dynamic contrast-enhanced (DCE) MRI is an established clinical imaging method for assessing hemodynamic parameters in tissue, showing promising clinical utility for cancer diagnosis and treatment monitoring (1,2). In the brain, numerous studies have shown the utility of DCE MRI to assess the altered hemodynamics and blood-brain-barrier (BBB) permeability associated with in a variety of brain pathologies (3,4) However, gadolinium-based contrast agents (GBCA) are limited to patients with normal kidney function (eGFR> 30 ml/min) because of the risk of developing nephrogenic systemic fibrosis (NSF) (5) and may result in gadolinium deposition (6,7), which, although rare, is an indication against GBCAs being used frequently and repetitively.

A number of sugars were recently developed as Chemical Exchange Saturation Transfer (CEST) MRI agents (8,9) with the hope to be used as the alternatives to GBCA to ameliorate

increasing safety concerns of the use of GBCA in some patient populations. For instance, D-glucose is being investigated as a biodegradable MRI contrast agent (10–13). Both preclinical(11,14) and human (13,15) studies have shown the capacity of dynamic glucose-enhanced (DGE) MRI to assess increased tumor blood volume and BBB dysfunction. Other glucose-derivatives, including 2-deoxy-D-glucose (2-DG) (16–18), 3-O-methyl-D-glucose (3OMG) (19–21), glucosamine (22), sucralose (23), sucrose (24), and glycogen (25,26) have also been investigated to pursue safe, CEST-based MRI contrast enhancement. Except for glycogen, all these molecules are small-molecular-weight molecules and most of them can be metabolized and some, for instance 2-DG, may result in unwanted cellular effects.

Recent studies have shown that dextrans have potential as a new class of CEST agents with several advantages (27–31). Dextrans are highly branched polymers of glucose and have been used clinically for more than six decades as plasma volume expanders, peripheral flow promotors, and anti-thrombolytic agents with a proven safety profile (32,33). Indeed, dextran 70 (dextran with MW ~ 70k) is on the WHO Model List of Essential Medicines. However, dextrans of high molecular weight (MW) have the risk to cause anaphylaxis or anaphylactoid reactions (34). To this end, we are interested in the smallest and safest dextran (MW= 1kDa, Dex1). Dex1 is available for medical use with the tradename of Promit® and has been approved by the FDA for reducing the incidence of high-MW-dextran-induced anaphylactoid/anaphylactic reactions (35). According to the latter report, a clinical survey among more than 8 million exposures in northern Europe over a period of more than 20 years shows that 20 mL Dex1 administration 15 minutes prior to the administration of LMD (dextran 40) could effectively reduce severe dextran-induced anaphylactoid/ic reaction by 35-fold (from 1:2000 to 1:70,000) and reduce fatal reactions by 90-fold. Used individually, no Dex1-caused allergic reactions have been reported before (35). Therefore, Dex1 can be considered the safest agent in the dextran family when given to patients as an injectable solution. In the present study, we aimed to investigate the ability of Dex1 to measure tumor hemodynamics in a mouse brain tumor model.

Experimental

Materials

Without otherwise noted, all chemicals were purchased from Sigma Aldrich (Saint Louis, MO, USA). Dextran1 (MW= 1 kDa, *abbr*. Dex1, USP grade) was purchased from Pharmacosmos (Denmark).

Tumor model

All animal studies were approved by our Institutional Animal Care and Use Committee. C57BL6 mice (female, 5–6 weeks, n=4) were stereotactically injected with 2×10^4 murine glioma GL261 cells at a depth of 3 mm below the dura mater, and orthotopic brain tumors were formed after 21 days to reach at the desirable size (3–5 mm in diameter).

In vitro MRI

Dex1 was dissolved in PBS buffer at different concentrations and pH values and studied with CEST MR using a vertical bore Bruker 11.7 T MRI scanner equipped with a 15 mm volume

coil and a horizontal bore 3T Bruker BioSpec system (Bruker, Ettlingen, Germany) equipped a 40-mm volume transceiver coil. Temperature was maintained at 37°C by an air heater. For 11.7T MRI,CEST MR images were acquired using a RARE sequence with a continuous wave pre-saturation pulse (B_1=1.8 μT, 3 sec) swept from −4 to +4 ppm (step=0.2 ppm) for the full Z-spectrum; TR/TE=6.0s/5 ms, RARE factor=16, slice thickness = 2 m, matrix size= 64×64, FOV = 16 × 16 mm^2, spatial resolution= 0.25×0.25 mm^2, number of average=2, total acquisition time= 16 min 48 s.

For 3T MRI, CEST MR images were acquired using the same RARE sequence with TR/TE= 6000/4.6 ms, B_1=1.8 μT/3 sec, saturation offsets= −5 to +5 ppm with an increment of 0.1 ppm between ±1 ppm and an increment of 0.2 ppm otherwise, slice thickness = 3 mm, matrix size= 64×64, FOV = 20 × 20 mm^2, spatial resolution= 0.31×0.31 mm^2, number of average=1, total acquisition time= 12 min 48 s. Prior to CEST MRI, B_0 was adjusted using the first-order B_0 shimming method and the resulted FWHM is on the order of <5 Hz. The WASSR method was used to compute and correct B_0 shifts pixel by pixel. Three images acquired at the offset of 200 ppm were used as the S_0 image for Z-spectrum normalization.

In vivo MRI

In vivo MRI was carried out on a Biospec 11.7 T horizontal MRI scanner equipped with a 23 mm mouse brain volume coil. The imaging protocol is shown in Figure 1. In brief, CEST acquisitions were preceded by a water saturation shift referencing (WASSR) scan, needed for B_0 inhomogeneity assessment and correction in the Z-spectrum (36). During the dynamic CEST acquisition, a pre-infusion period (2 min) was included to acquire baseline signal. Then, 200 μL of Dex1 solution (250 mg/mL in saline) was then i.v. infused for 1 min (dose= 2 g/kg, injection rate= 1.67 μL/s), followed by flushing using 50 μL saline (dead volume= 50 μL). Post-infusion acquisition was long ~20 min. All CEST MR images were acquired using a modified fat-suppressed RARE sequence (CW saturation pulse: B_1=1.8 μT, 3 s, TR/TE=5000/5 ms, RARE factor=23, matrix size= 64 × 64 (with partial FT acceleration to 64 × 23), spatial resolution= 0.28 × 0.25 mm^2, slice thickness = 1 mm, number of average NA=2, acquisition time=7 min). Steady-state Z-spectral acquisitions were acquired from −4 to +4 ppm (0.2 ppm steps) before and 20 minutes after Dex1 injection. Dynamic dextran enhanced (DDE) MRI was acquired repeatedly at the single frequency offset of 1.2 ppm relative to the water proton resonance at a temporal resolution of 10 s for 20 minutes.

Animals were also examined by DCE MRI with *i.v.* injection of ProHance® (0.1 mmol/kg, bolus over about 10 s, injection volume =50 μL, injection rate= 5 μL/s). A single-slice FLASH gradient echo sequence (TR/TE=18/3 ms, and flip angle =15°) was used to acquire DCE images at the same position and spatial resolution as the CEST images. The acquisition started one minute before injection. The total acquisition time of DCE MRI was 13 min, and the temporal resolution was 14.6 s.

Synthesis of fluorescent Dex1

Cy5.5-labeled Dex1 was synthesized according to a previously reported route (28). Briefly, 0.4 μmol of Dex1 in DMSO (1.5 mL), 0.22 μmol of N,N′-Disuccinimidyl carbonate (DSC) in 1 mL of DMSO, and triethylamine (TEA) (10 μL) were mixed and stirred for

20 h at room temperature. The activated Dex1 was collected by centrifuging at 4000 × g for 5 min after dropping the reaction mixture to cold acetone, and conjugated with Cy5.5-amine (Lumiprobe, Cat#470C0, Hunt Valley, MD, USA) at the molar ratio of Dex1:Cy5.5-amine=1:3 in DMSO for overnight, catalyzed by five equiv. of anhydrous N,N-diisopropylethyl amine (DIPEA). The final product was precipitated in acetone, collected by centrifugation, and washed with acetone.

Immunofluorescence

Tumor-bearing mice were *i.v.* injected with 10 μg (~ 72 nmol) Dex1-Cy5.5 (200 μL of 0.36 mM in saline solution). One hour later, mice were sacrificed, and the brains were harvested, frozen, and cryosectioned at a thickness of 5 μm. Tissue slides were counterstained with DAPI (Sigma). Images of the brain section were acquired using a Zeiss Axiovert 200 base microscope.

Data processing

Both *in vitro* and in *vivo* MRI data were processed using custom-written MATLAB scripts. The magnetization transfer ratio asymmetry was used to quantify the CEST effects with respect to saturation offset, which is defined as $MTR_{asym}=(S^{-\Delta\omega} - S^{+\Delta\omega})/S_{0,}$ where $S^{+\Delta\omega}$ and $S^{-\Delta\omega}$ are the MRI signals with RF irradiation at the offsets of $+\Delta\omega$ and $-\Delta\omega$ relative to the water resonance, respectively, and S_0 is the signal acquired without RF saturation. After correcting the Z-spectral frequency for B_0 inhomogeneity using the WASSR method, the *in vivo* steady-state CEST contrast was quantified by $MTR_{asym} = (S^{-\Delta\omega} - S^{+\Delta\omega})/S_0$ at 1.2 ppm. Before and after DDE, the change in CEST signal was quantified by $\Delta MTR_{asym} = MTR_{asym}(post) - MTR_{asym}(pre)$.

For the pharmacokinetic analysis, the DDE and DCE data between 0–10 min post-injection were used, with the time 0 referred to the time point where injection was started. The data were first subtracted by the corresponding baseline contrast, calculated by averaging the pre-injection CEST and T_{1w} contrast between −2 to 0 min (number of acquisitions= 20) and −1 to 0 min (number of acquisitions =2) for DDE and DCE, respectively.

When a single offset (1.2 ppm) approach was used, as the CEST effect causes water signal to reduce, the dynamic CEST contrast enhancement was calculated by the absolute values of MR signal decrease, *i.e.*, $\Delta S(t)^{1.2ppm}/S_0 = [S(t=0)^{1.2ppm}/S_0 - S(t)^{1.2ppm}/S_0] \times 100\%$. For DCE data, the concentration of Gd was calculated by the $\Delta S(t)/S_0$% (Supplementary method) as previously described (30). Area-under-curve (AUC) maps for both DDE and DCE images were calculated by integrating the calculated contrast-enhancement images (i.e., $\Delta S(t)^{1.2ppm}/S_0$ % and mM [Gd] for DDE and DCE, respectively) over a period of the 0–10 min after injection using the MATLAB built-in trapezoid function pixel-by-pixel. The averaged pre-injection signals were used as baseline.

Statistical analysis

Data were expressed as mean ± SD unless otherwise stated. The comparison of two groups was conducted using unpaired two-tailed Student's t-test. Bland-Altman analysis (37) was also performed to assess the agreement between DCE and DDE methods, with a criteria of

95% of the standard deviation of the differences between the two methods. Differences with $P<0.05$ were considered statistically significant.

Results:

CEST characteristics of dextran1

The chemical structure of Dex1 is shown in Figure 2A, which contains on average 6 glucose units and each glucose unit contains 3 hydroxyl protons (38). We first used conventional ^{1}H NMR to confirm the chemical shifts of the exchangeable hydroxyl protons. In Figure 2B, the NMR spectra of 100 mM Dex1 acquired in D_2O and H_2O (pH 6.5 and 20 °C to reduce exchange rate) are compared, showing that the hydroxyl protons appear over a range 5.5 −6 ppm in the ^{1}H spectrum, which is *about*. 0.8–1.3 ppm relative to the water resonance frequency (4.7 ppm in the ^{1}H NMR spectrum). In the Z-spectrum, these protons appear as a broad CEST signal between 0.5 to 2 ppm with the apparent CEST peak maximum frequency highly dependent on the B_1 field strength (Figs. S1A,B) due to interference of direct water saturation. Similar to glucose and other dextrans (30), the CEST signal of Dex1 depends strongly on pH (Figs. 2C,D). For the pH range studied, CEST signal decreases with increased pH. As the exchange rate of hydroxyl protons was observed to continuously increase over the range pH 6–8 (as calculated by their T_2 relaxation times, supplementary Methods S1 and Figure S2), the reduction in CEST contrast can be explained by the fact the exchange rate goes from the slow to intermediate to fast exchange regime compared to $\Delta\omega = 1.2\ \text{ppm} \times 500 \times 2\pi = \sim 3768$ rad/s. The increase exchange rate also generates a pH-dependent T_{2ex} enhancing effect (relaxivity of 0.195 $s^{-1}mM^{-1}$, Figures S3A and S3B), whereas negligible T_1 enhancement was observed (Figures S3C and S3D). At the same glucose unit concentration, the CEST contrast of Dex1 at ~1.2 ppm is comparable to that of glucose, whereas CEST peaks of other hydroxyl protons (2–3 ppm) of D-glucose disappear in Dex1 due to polymerization (Fig. 2E). Considering that the glucose unit in Dex1 has a MW of 162, this result reveals that the detectability of Dex1 (MW= 1 kDa, containing 6 glucose units) is approximately six times higher than the CEST signal of glucose at 1.2 ppm on a per molecule basis. Finally, to verify if the single offset approach can be used for acquiring dynamic CEST at a high temporal resolution, we plotted the $(1- S^{1.2ppm}/S_0)$ vs. concentration (Fig. 2F), which shows a good linear relationship in the range of 2 – 40 mM (per glucose unit). The dexCEST contrast is still substantial for pH values below 7 at 3T (Fig. 3 A–C). Compared to 11.7T, the detectability of Dex1 at 3T was lower as a result of the decreased chemical shift (in units of Hz) with respect to water) and shortened T_1 relaxation times at lower fields (Fig. 3D).

Dex1-based contrast-enhanced CEST MRI in brain tumors

We first compared the Z-spectra before and at 20 minutes post-administration of Dex1. As shown in Figure 4A, there was a substantial CEST contrast enhancement in the tumor, in good agreement with contrast-enhanced (CE) image obtained by Gd-DOTA. Interestingly, there were also some areas showing noticeable CEST contrast outside tumor but the magnitude of contrast enhancement was much weaker. The comparison of pre- and post-injection mean ROI CEST contrast (Figs. 4B–C) revealed a significantly elevated CEST contrast at 1.2 ppm in the tumor (Fig. 4D, $P=0.0201$) but not in contralateral brain (Fig.

4E, P=0.6290). The contrast enhancement in the tumor for five mice was significantly higher than that in the brain (ΔMTR_{asym}=0.010 ±0.006 and 0.002±0.008, respectively, P=0.0069, Fig. 4F). The selected tumor uptake of Dex1 was also confirmed by fluorescence microscopy, where a much higher intensity of red fluorescence (Dex1-Cy5.5) was observed in the tumor bed than that outside tumor rim (Figs. 4G, S4). Higher steady-state CEST MRI contrast enhancement in the tumor than in the brain was observed in all five mice studied (Fig. S5).

Contrast enhancement in the tumor assessed by DDE MRI

We also acquired dynamic dextran-enhanced (DDE) CEST MRI during the first 20 minutes after injection of Dex1 according to the image scheme in Figure 1. To illustrate the dynamic changes, three ROIs (tumor, contralateral brain, and ventricle) were drawn manually based on the T_2-weighted anatomical images (Fig. 5A). As shown in Figure 5B, the injection of Dex1 induced a substantial CEST enhancement ($\Delta S^{1.2ppm}/S_0$) in the tumor, whereas a much lower, initially negative effect was observed in contralateral brain and ventricle. To ensure the dexCEST contrast was not caused by the change in B_0 inhomogeneity, we also measured the ΔB_0 shifts after Dex1 infusion, which were determined to be negligible in majority of the brain and not substantially different between tumor and brain parenchyma (Fig. S6). Using the dynamic curve, one can calculate the area-under-curve (AUC) between 0–10 min. As can be seen in Figure 5C, the AUC images showed clear tumor enhancement. Among four mice studied with DDE MRI, the mean AUC(0–10min) values in the tumor and contralateral brain ROIs were 21.9±4.2 and 5.3±6.4 %·min, respectively (Fig. 5D, P=0.0294, paired Student's t-test). The Gd-based DCE MRI also showed strong contrast enhancement in the tumor but not in the brain (Figs. 5E, 5F). For DCE, the average AUC(0–10min) values were 0.75 ± 0.27 and −0.07 ± 0.10 mM·min for tumor and contralateral brain, respectively (paired Student's t-test, P=0.0203, Fig.5G). Of note, there was a low but noticeable signal loss in the contralateral normal hemisphere and ventricles, attributed to the circulating Gd contrast agent in the blood vessels leading to a T2* effect. Since the T_2* effect is more pronounced at higher magnetic field, there will be a significant decreased MRI intensity, which counteracts the T_1 effect caused by the Gd contrast agent (39). The observation of a T_2* effect in the contralateral hemisphere indicates that, when assuming a linear relationship between MRI intensity and Gd agent concentration, the quantification of concentration in the tumor may lead to underestimation since a T_2* effect would also occur in the tumor when the Gd contrast agent enters the extravascular space (40).

We also conducted DDE MRI in non-tumor bearing mice (Figs. 6, S7). The result shows a negligible contrast enhancement in the non-tumor-bearing normal brain (Fig. 6B). As shown in Figure 6C, the mean AUC (0–10 min) value in the similar regions (indicated in Fig. 6A and Fig. 5A) in the brains of non-tumor bearing mice was determined to be −1.59 ± 2.43 %·min, which is lower than that of the normal brain in tumor-bearing mice (*i.e.*, 5.3±6.4 %·min, unpaired Student's t-test, P=0.143).

Discussion

Our study shows that Dex1 has potential as a non-chemically-labeled, diamagnetic CEST agent for tumor hemodynamic characterization, *i.e.*, assessment of perfusion and permeability properties. Recently, we (29,30,41) and others (27) have demonstrated that dextrans of different MW can be used as CEST contrast agents. Dextrans cannot be metabolized by most mammalian cells (42,43), and hence are suitable for being used as contrast agents with a relatively longer blood lifetime than small molecular imaging agents such as D-glucose. Different from our previous studies where dextrans of high MW were used, the present study employed Dex1, the smallest and safest form of dextran, which may ease future clinical translation. Dex1 (Promit®) has been approved by the FDA as an intravenous injectable agent for effectively reducing the chance of an allergic reaction to dextran-based fluids, such as dextran 40 and dextran 70 (35,44). Studies have shown that Dex1 is biologically inert and can be eliminated from blood circulation rather quickly. For example, Schwarz et al reported that the a mean elimination half-time of Dex1 was only 1.9 h in healthy subjects, whereas that of Dex40 is around 9.5 h, and more than 77% of administered Dex1 was excreted through urine in 6 hours without metabolic changes (42). Our *in vitro* result showed that Dex1 generates approximately same CEST contrast as D-glucose on a per weight/volume concentration basis, or 6-time higher on a per molecule basis. As glucose-enhanced CEST MRI has been tested on 3T clinical scanners recently (12,13), Dex1 may be also potentially clinically useful, given the similarity between the CEST MRI properties and detectability between Dex1 and D-glucose. As a first demonstration, the present study systemically investigated the ability of Dex1 as an MRI contrast agent to detect and characterize brain tumors.

Like Gd-based DCE MRI, Dex1-based DDE MRI provides a quantitative measure of the tumor hemodynamics. In our study, we analyzed DDE data using the AUC values between 0–10 minutes and compared them to DCE. The AUC analysis is a widely used model-free method for quantifying the regional uptake of diagnostic or therapeutic agents (45) and is particularly suitable for assessing BBB integrity (46). Indeed, the AUC method has been used by us (14,15) and others (11) in dynamic glucoCEST MRI studies. AUC analysis of DDE MRI provided a quantitative assessment of the increased tumor uptake of Dex1, reflecting most likely a combined effect of increase blood volume and disrupted BBB in the tumor, which was consistent with DCE MRI.

As one of the most abundant types of exchangeable protons, the hydroxyl proton has drawn strong interest for generating CEST contrast (8). For example, D-glucose is being extensively studied as a safe agent for tumor detection, which has entered human testing recently (12,15,47). In addition to D-glucose, other glucose analogs are being investigated as CEST agents on different mouse tumor models (18–22). The contrast between tumor and normal tissues is reflective of higher tumor uptake and accumulation of these agents, attributable to the hemodynamic changes such as perfusion, increased blood volume, vascular permeability and BBB integrity (14,48), and pathological changes such as, for some sugars, overexpressed glucose transporters (49). Compared to those agents, dextrans are non-metabolizable and BBB impermeable, hence more suitable for assessing BBB integrity. In fact, fluorescently labeled dextrans of various sizes have been widely used in preclinical

studies to assess BBB permeability (50–52). Our study also shows that the intravenously infused Dex1 preferentially extravasated in the brain tumor, providing an effective way to characterize the altered hemodynamics associated with tumor pathology. More importantly, our results showed that the dexCEST contrast is substantial at low pHs (i.e., pH < 7) at 3T, Therefore, it is feasible to use dexCEST MRI at 3T to detect tumors where extracellular extravascular space pH is acidic(53). Hence, Dex1 may be used as a substitute for Gd-based agents for detecting BBB dysfunction. While the molecular weights for Dex1 (1kDa) and Gd-DOTA (559 Da) are very similar, the experiments show different pharmacokinetics, indicating that other factors are relevant. These could for instance be conformation/shape and surface charge/hydrophilicity. Although of the same order of magnitude, the MW of Dex1 (1 kDa) is still almost double that of Gd-DOTA (559 Da); Also, dextran is a branched polymer and has inherently great flexibility and high degrees of conformational freedom due to its α-1,6-linkages(54), whereas Gd-DOTA is a monomer with well-defined more rigid structural conformation. On the other hand, different injection rates and volumes were used for Dex1 and Gd-DOTA, which also contribute to the different tracer kinetics between the two agents. For example, Dex1 was infused over 1 min at an injection rate of 1.67 μL/s (total volume =100 μL), whereas Prohance was injected as a bolus within 10 s at an injection rate of 5 μL/s (50 μL). Figure S8 shows the estimation of the time dependent (arterial and venous) blood concentrations of Dex1 and Gd-DOTA, indicating the two agents have different arterial-input and venous-output functions and thus may have different response curves. All these factors may contribute to the difference in MRI contrast appearance between the two agents. Nevertheless, our study has demonstrated the utility of Dex1-based CEST MRI for hemodynamic assessment. Future optimization of acquisition parameters and data processing methods are warranted to fully harness the ability of Dex1-based CEST MRI to characterize the hemodynamic properties of brain tumors.

Surprisingly, both CEST MRI and immunofluorescence results indicate there was a low but detectable quantity of Dex1 in some supposedly normal brain regions in the tumor-bearing mice. While the exact reasons are still under investigation, we speculate that these regions are not completely normal and may have subtle changes as no significant CEST MRI contrast was observed in the brain of non-tumor bearing mice after injection of Dex1 at the same dose. One possible reason is that Dex1 can be taken up in CSF through a disrupted CSF barrier and sequentially diffuse to other parts of the brain. For example, Kress et al showed in their study that the exchange of fluorescently labeled 3 kDa dextran between CSF and brain parenchyma was pronounced in young and middle age mice (55). It is also possible that these areas were affected by tumor infiltration or systemic inflammatory reactions. In fact, we used the C57BL/6 syngeneic cell line GL261 to form intracranial tumors, which, unlike the commonly used 9L and U87 mouse models, exhibit rapid growth and invasive growth pattern similar to the human disease and often have margins that are not sharply delineated as tumor cells infiltrate into the surrounding brain tissues. Of note, dextran is a clinical plasma expander, and the administration of Dex1 in our study may cause transiently increased cerebral blood volume (CBV) (56) and flow (CBF) (57). Moreover, Dex1, if infused at a high dose may cause increased blood glucose level (58). Those effects may also lead to changes in the CEST contrast, and sometimes cause negative effect (decrease of CEST signal at 1.2 ppm)(48,59). Another technical challenge for dynamic

CEST contrast enhancing MRI is the transient effect of contrast injection. For instance, in our study, the injection volume of Dex1 solution is 150 μL, which would cause a 7.5% blood volume increase, assuming the total blood volume in a mouse is 2 mL. Given the T_1 and T_2 relaxation times of saline (3) are substantially different from those of blood at 11.7 T (60,61), the injection can result in noticeable change in MRI intensity and frequency (BOLD effect) and lead to misinterpretation if only the change in MRI signal at a single offset (i.e., S(1.2ppm)/S_0 in the present study) is used to quantify CEST contrast. Hence, our AUC results contain a small but non-negligible error raised from the injection itself. On the other hand, the Z-spectral approach can provide a more reliable quantitative measurement of Dex1 because the MTR_{asym} analysis after B0 field correction can effectively compensate for the T_1 and T_2 effects, and the body fluid equilibrium can be resumed after a few minutes. Further investigation of these potentially confounding effects is warranted.

Our study used a dynamic continuous wave CEST acquisition scheme to assess the signal change at a single offset (i.e., 1.2 ppm). Of note, hydroxyl protons of sugars can also be detected by other chemical exchange-sensitive MRI contrast methods, including $T_{1\rho}$ (spin lock) (e.g., for glucose (12) and 3-OMG (48)), T_{2ex} (e.g., for glycogen (62), glucose(63), and D-maltose (64)), and on-resonance variable delay multiple pulse (onVDMP) (e.g., for glucose (65)). Compared to the standard off-resonance CEST approach, these alternative methods may provide higher contrast in the detection of hydroxyl protons whose exchange rate falls into the intermediate to fast exchange regime. We will investigate the potential of these methods in the detection of dextrans in our future studies.

In summary, we explored the smallest form of dextran, Dex1, as a new MRI contrast agent and applied it to assess brain tumor hemodynamics. Our results showed the intravenously injected Dex1 led to a substantial CEST MRI contrast enhancement in the tumor but not in the brain. Pharmacokinetic analysis of dynamic dextran-enhanced MRI data revealed the high uptake of Dex1 is due to the augmented vascular permeability in the tumor, in good agreement with Gd-based DCE MRI and fluorescence microscopy. As Dex1 has an excellent safety profile, it has great potential to be developed towards a clinically useful MRI contrast agent.

Supplementary Material

Refer to Web version on PubMed Central for supplementary material.

Acknowledgments

This work was supported by NIH grants R01CA211087, R21CA215860, R01EB019934, the Swedish Research Council grants: 2015-04170, 2019-03637, and the Swedish Cancer Society grants: CAN 2015/251, CAN 2018/550.

Abbreviations

CBF	cerebral blood volume flow
CBV	cerebral blood volume
CEST	Chemical Exchange Saturation Transfer

DDE	Dynamic dextran-enhanced
DCE	Dynamic contrast-enhanced
BBB	blood-brain-barrier
GBCA	gadolinium-based contrast agent
NSF	nephrogenic systemic fibrosis
DGE	dynamic glucose-enhanced
2-DG	2-deoxy-D-glucose
3OMG	3-O-methyl-D-glucose
WASSR	N,N-diisopropylethyl amine
TEA	triethylamine
DSC	N,N′-Disuccinimidyl carbonate
AUC	Area-under-curve
onVDMP	on-resonance variable delay multiple pulse
AIF	arterial input function

References

1. Knopp MV, Giesel FL, Marcos H, von Tengg-Kobligk H, Choyke P. Dynamic contrast-enhanced magnetic resonance imaging in oncology. Top Magn Reson Imaging 2001;12(4):301–308. [PubMed: 11687716]
2. Zhang J, Liu H, Tong H, Wang S, Yang Y, Liu G, Zhang W. Clinical Applications of Contrast-Enhanced Perfusion MRI Techniques in Gliomas: Recent Advances and Current Challenges. Contrast Media Mol Imaging 2017;2017:7064120. [PubMed: 29097933]
3. Larsson HB, Stubgaard M, Frederiksen JL, Jensen M, Henriksen O, Paulson OB. Quantitation of blood-brain barrier defect by magnetic resonance imaging and gadolinium-DTPA in patients with multiple sclerosis and brain tumors. Magn Reson Med 1990;16(1):117–131. [PubMed: 2255233]
4. Heye AK, Culling RD, Valdes Hernandez Mdel C, Thrippleton MJ, Wardlaw JM. Assessment of blood-brain barrier disruption using dynamic contrast-enhanced MRI. A systematic review. Neuroimage Clin 2014;6:262–274. [PubMed: 25379439]
5. Marckmann P, Skov L, Rossen K, Dupont A, Damholt MB, Heaf JG, Thomsen HS. Nephrogenic systemic fibrosis: suspected causative role of gadodiamide used for contrast-enhanced magnetic resonance imaging. J Am Soc Nephrol 2006;17(9):2359–2362. [PubMed: 16885403]
6. Malayeri AA, Brooks KM, Bryant LH, Evers R, Kumar P, Reich DS, Bluemke DA. National Institutes of Health perspective on reports of Gadolinium deposition in the brain. J Am Coll Radiol 2016;13(3):237–241. [PubMed: 26810815]
7. Stanescu AL, Shaw DW, Murata N, Murata K, Rutledge JC, Maloney E, Maravilla KR. Brain tissue gadolinium retention in pediatric patients after contrast-enhanced magnetic resonance exams: pathological confirmation. Pediatr Radiol 2020;50(3):388–396. [PubMed: 31989188]
8. Han Z, Liu G. Sugar-based biopolymers as novel imaging agents for molecular magnetic resonance imaging. Wiley Interdiscip Rev Nanomed Nanobiotechnol 2019;11(4):e1551. [PubMed: 30666829]
9. Rivlin M, Navon G. Molecular imaging of tumors by chemical exchange saturation transfer MRI of glucose analogs. Quant Imaging Med Surg 2019;9(10):1731–1746. [PubMed: 31728315]

10. Chan KW, McMahon MT, Kato Y, Liu G, Bulte JW, Bhujwalla ZM, Artemov D, van Zijl PC. Natural D-glucose as a biodegradable MRI contrast agent for detecting cancer. Magn Reson Med 2012;68(6):1764–1773. [PubMed: 23074027]
11. Walker-Samuel S, Ramasawmy R, Torrealdea F, Rega M, Rajkumar V, Johnson SP, Richardson S, Goncalves M, Parkes HG, Arstad E, Thomas DL, Pedley RB, Lythgoe MF, Golay X. In vivo imaging of glucose uptake and metabolism in tumors. Nat Med 2013;19(8):1067–1072. [PubMed: 23832090]
12. Herz K, Lindig T, Deshmane A, Schittenhelm J, Skardelly M, Bender B, Ernemann U, Scheffler K, Zaiss M. T1rho-based dynamic glucose-enhanced (DGErho) MRI at 3 T: Method development and early clinical experience in the human brain. Magn Reson Med 2019;82(5):1832–1847. [PubMed: 31231853]
13. Xu X, Sehgal AA, Yadav NN, Laterra J, Blair L, Blakeley J, Seidemo A, Coughlin JM, Pomper MG, Knutsson L, van Zijl PCM. d-glucose weighted chemical exchange saturation transfer (glucoCEST)-based dynamic glucose enhanced (DGE) MRI at 3T: early experience in healthy volunteers and brain tumor patients. Magn Reson Med 2020;84(1):247–262. [PubMed: 31872916]
14. Xu X, Chan KW, Knutsson L, Artemov D, Xu J, Liu G, Kato Y, Lal B, Laterra J, McMahon MT, van Zijl PC. Dynamic glucose enhanced (DGE) MRI for combined imaging of blood-brain barrier break down and increased blood volume in brain cancer. Magn Reson Med 2015;74(6):1556–1563. [PubMed: 26404120]
15. Xu X, Yadav NN, Knutsson L, Hua J, Kalyani R, Hall E, Laterra J, Blakeley J, Strowd R, Pomper M, Barker P, Chan K, Liu G, McMahon MT, Stevens RD, van Zijl PC. Dynamic Glucose-Enhanced (DGE) MRI: Translation to Human Scanning and First Results in Glioma Patients. Tomography : a journal for imaging research 2015;1(2):105–114.
16. Jin T, Mehrens H, Wang P, Kim SG. Glucose metabolism-weighted imaging with chemical exchange-sensitive MRI of 2-deoxyglucose (2DG) in brain: Sensitivity and biological sources. Neuroimage 2016;143:82–90. [PubMed: 27570111]
17. Nasrallah FA, Pages G, Kuchel PW, Golay X, Chuang KH. Imaging brain deoxyglucose uptake and metabolism by glucoCEST MRI. J Cereb Blood Flow Metab 2013;33(8):1270–1278. [PubMed: 23673434]
18. Rivlin M, Horev J, Tsarfaty I, Navon G. Molecular imaging of tumors and metastases using chemical exchange saturation transfer (CEST) MRI. Sci Rep 2013;3:3045. [PubMed: 24157711]
19. Rivlin M, Navon G. CEST MRI of 3-O-methyl-D-glucose on different breast cancer models. Magn Reson Med 2018;79(2):1061–1069. [PubMed: 28497566]
20. Rivlin M, Tsarfaty I, Navon G. Functional molecular imaging of tumors by chemical exchange saturation transfer MRI of 3-O-Methyl-D-glucose. Magn Reson Med 2014;72(5):1375–1380. [PubMed: 25236979]
21. Sehgal AA, Li Y, Lal B, Yadav NN, Xu X, Xu J, Laterra J, van Zijl PCM. CEST MRI of 3-O-methyl-D-glucose uptake and accumulation in brain tumors. Magn Reson Med 2019;81(3):1993–2000. [PubMed: 30206994]
22. Rivlin M, Navon G. Glucosamine and N-acetyl glucosamine as new CEST MRI agents for molecular imaging of tumors. Sci Rep 2016;6:32648. [PubMed: 27600054]
23. Bagga P, Haris M, D'Aquilla K, Wilson NE, Marincola FM, Schnall MD, Hariharan H, Reddy R. Non-caloric sweetener provides magnetic resonance imaging contrast for cancer detection. J Transl Med 2017;15(1):119. [PubMed: 28558795]
24. Longo DL, Moustaghfir FZ, Zerbo A, Consolino L, Anemone A, Bracesco M, Aime S. EXCI-CEST: Exploiting pharmaceutical excipients as MRI-CEST contrast agents for tumor imaging. Int J Pharm 2017;525(1):275–281. [PubMed: 28433532]
25. van Zijl PC, Jones CK, Ren J, Malloy CR, Sherry AD. MRI detection of glycogen in vivo by using chemical exchange saturation transfer imaging (glycoCEST). Proc Natl Acad Sci U S A 2007;104(11):4359–4364. [PubMed: 17360529]
26. Zhou Y, van Zijl PCM, Xu X, Xu J, Li Y, Chen L, Yadav NN. Magnetic resonance imaging of glycogen using its magnetic coupling with water. Proc Natl Acad Sci U S A 2020;117(6):3144–3149. [PubMed: 32001509]

27. Cobb JG, Li K, Xie J, Gochberg DF, Gore JC. Exchange-mediated contrast in CEST and spin-lock imaging. Magn Reson Imaging 2014;32(1):28–40. [PubMed: 24239335]
28. Han Z, Zhang S, Fujiwara K, Zhang J, Li Y, Liu J, van Zijl PCM, Lu ZR, Zheng L, Liu G. Extradomain-B Fibronectin-Targeted Dextran-Based Chemical Exchange Saturation Transfer Magnetic Resonance Imaging Probe for Detecting Pancreatic Cancer. Bioconjug Chem 2019;30(5):1425–1433. [PubMed: 30938983]
29. Chen H, Liu D, Li Y, Xu X, Xu J, Yadav NN, Zhou S, van Zijl PCM, Liu G. CEST MRI monitoring of tumor response to vascular disrupting therapy using high molecular weight dextrans. Magn Reson Med 2019;82(4):1471–1479. [PubMed: 31106918]
30. Li Y, Qiao Y, Chen H, Bai R, Staedtke V, Han Z, Xu J, Chan KWY, Yadav N, Bulte JWM, Zhou S, van Zijl PCM, Liu G. Characterization of tumor vascular permeability using natural dextrans and CEST MRI. Magn Reson Med 2018;79(2):1001–1009. [PubMed: 29193288]
31. Liu G, Ray Banerjee S, Yang X, Yadav N, Lisok A, Jablonska A, Xu J, Li Y, Pomper MG, van Zijl P. A dextran-based probe for the targeted magnetic resonance imaging of tumours expressing prostate-specific membrane antigen. Nat Biomed Eng 2017;1(12):977–982. [PubMed: 29456877]
32. Dubick MA, Wade CE. A review of the efficacy and safety of 7.5% NaCl/6% dextran 70 in experimental animals and in humans. Journal of Trauma-Injury, Infection, and Critical Care 1994;36(3):323–330.
33. Thorén L The dextrans--clinical data. Developments in biological standardization 1980;48:157–167. [PubMed: 6168501]
34. Zinderman CE, Landow L, Wise RP. Anaphylactoid reactions to Dextran 40 and 70: reports to the United States Food and Drug Administration, 1969 to 2004. J Vasc Surg 2006;43(5):1004–1009. [PubMed: 16678697]
35. Ljungstrom KG. Dextran 40 therapy made safer by pretreatment with dextran 1. Plast Reconstr Surg 2007;120(1):337–340. [PubMed: 17572583]
36. Kim M, Gillen J, Landman BA, Zhou J, van Zijl PC. Water saturation shift referencing (WASSR) for chemical exchange saturation transfer (CEST) experiments. Magn Reson Med 2009;61(6):1441–1450. [PubMed: 19358232]
37. Bland J, Altman D. Statistical methods for assessing agreement between two methods of clinical measurement. Lancet 1986;1(8476):307–310. [PubMed: 2868172]
38. Sabadini E, do Carmo Egidio F, Fujiwara FY, Cosgrove T. Use of water spin-spin relaxation rate to probe the solvation of cyclodextrins in aqueous solutions. J Phys Chem B 2008;112(11):3328–3332. [PubMed: 18303884]
39. Kim J, Moestue SA, Bathen TF, Kim E. R2* Relaxation Affects Pharmacokinetic Analysis of Dynamic Contrast-Enhanced MRI in Cancer and Underestimates Treatment Response at 7 T. Tomography 2019;5(3):308–319. [PubMed: 31572792]
40. Ewing JR, Bagher-Ebadian H. Model selection in measures of vascular parameters using dynamic contrast-enhanced MRI: experimental and clinical applications. NMR Biomed 2013;26(8):1028–1041. [PubMed: 23881857]
41. Liu G, Banerjee SR, Yang X, Yadav N, Lisok A, Jablonska A, Xu J, Li Y, Pomper MG, van Zijl P. A dextran-based probe for the targeted magnetic resonance imaging of tumours expressing prostate-specific membrane antigen. Nat Biomed Eng 2017;1(12):977–982. [PubMed: 29456877]
42. Schwarz JA, Koch W, Buhler V, Kaumeier S. Pharmacokinetics of low molecular (monovalent) dextran (Dx 1) in volunteers. Int J Clin Pharmacol Ther Toxicol 1981;19(8):358–367. [PubMed: 6171533]
43. Loftsson T. Physicochemical Properties and Pharmacokinetics. In: Loftsson T, editor. Essential Pharmacokinetics;DOI:10.1016/b978-0-12-801411-0.00003-2. Boston: Academic Press; 2015. p 85–104.
44. Dubick MA, Wade CE. A review of the efficacy and safety of 7.5% NaCl/6% dextran 70 in experimental animals and in humans. J Trauma 1994;36(3):323–330. [PubMed: 7511708]
45. Heye AK, Thrippleton MJ, Armitage PA, Valdes Hernandez MDC, Makin SD, Glatz A, Sakka E, Wardlaw JM. Tracer kinetic modelling for DCE-MRI quantification of subtle blood-brain barrier permeability. Neuroimage 2016;125:446–455. [PubMed: 26477653]

46. Chu PC, Chai WY, Hsieh HY, Wang JJ, Wey SP, Huang CY, Wei KC, Liu HL. Pharmacodynamic analysis of magnetic resonance imaging-monitored focused ultrasound-induced blood-brain barrier opening for drug delivery to brain tumors. Biomed Res Int 2013;2013:627496. [PubMed: 23607093]
47. Xu X, Sehgal AA, Yadav NN, Laterra J, Blair L, Blakeley J, Seidemo A, Coughlin JM, Pomper MG, Knutsson L, van Zijl PCM. D-glucose weighted chemical exchange saturation transfer (glucoCEST)-based dynamic glucose enhanced (DGE) MRI at 3T: Early experience in healthy volunteers and brain tumor patients. Magn Reson Med 2019;DOI:10.1002/mrm.28124.
48. Jin T, Mehrens H, Wang P, Kim SG. Chemical exchange-sensitive spin-lock MRI of glucose analog 3-O-methyl-d-glucose in normal and ischemic brain. J Cereb Blood Flow Metab 2018;38(5):869–880. [PubMed: 28485194]
49. Xu X, Xu J, Knutsson L, Liu J, Liu H, Li Y, Lal B, Laterra J, Artemov D, Liu G, van Zijl PCM, Chan KWY. The effect of the mTOR inhibitor rapamycin on glucoCEST signal in a preclinical model of glioblastoma. Magn Reson Med 2019;81(6):3798–3807. [PubMed: 30793789]
50. Hoffmann A, Bredno J, Wendland M, Derugin N, Ohara P, Wintermark M. High and Low Molecular Weight Fluorescein Isothiocyanate (FITC)-Dextrans to Assess Blood-Brain Barrier Disruption: Technical Considerations. Transl Stroke Res 2011;2(1):106–111. [PubMed: 21423333]
51. Tervo T, Joo F, Palkama A, Salminen L. Penetration barrier to sodium fluorescein and fluorescein-labelled dextrans of various molecular sizes in brain capillaries. Experientia 1979;35(2):252–254. [PubMed: 421851]
52. Choi JJ, Wang S, Tung YS, Morrison B 3rd, Konofagou EE. Molecules of various pharmacologically-relevant sizes can cross the ultrasound-induced blood-brain barrier opening in vivo. Ultrasound Med Biol 2010;36(1):58–67. [PubMed: 19900750]
53. Hao G, Xu ZP, Li L. Manipulating extracellular tumour pH: an effective target for cancer therapy. RSC Advances 2018;8(39):22182–22192.
54. Brant DA, Liu HS, Zhu ZS. The dependence of glucan conformational dynamics on linkage position and stereochemistry. Carbohydr Res 1995;278(1):11–26. [PubMed: 8536263]
55. Kress BT, Iliff JJ, Xia M, Wang M, Wei HS, Zeppenfeld D, Xie L, Kang H, Xu Q, Liew JA, Plog BA, Ding F, Deane R, Nedergaard M. Impairment of paravascular clearance pathways in the aging brain. Ann Neurol 2014;76(6):845–861. [PubMed: 25204284]
56. Todd MM, Weeks JB, Warner DS. The influence of intravascular volume expansion on cerebral blood flow and blood volume in normal rats. Anesthesiology 1993;78(5):945–953. [PubMed: 8489067]
57. Namgung B, Ng YC, Nam J, Leo HL, Kim S. Alteration of Blood Flow in a Venular Network by Infusion of Dextran 500: Evaluation with a Laser Speckle Contrast Imaging System. PLoS One 2015;10(10):e0140038. [PubMed: 26466371]
58. Patki A, Shelgaonkar V. Effect of 6% hydroxyethyl starch-450 and low molecular weight dextran on blood sugar levels during surgery under subarachnoid block: A prospective randomised study. Indian J Anaesth 2010;54(5):448–452. [PubMed: 21189884]
59. Huang J, van Zijl PCM, Han X, Dong CM, Cheng GWY, Tse KH, Knutsson L, Chen L, Lai JHC, Wu EX, Xu J, Chan KWY. Altered d-glucose in brain parenchyma and cerebrospinal fluid of early Alzheimer's disease detected by dynamic glucose-enhanced MRI. Sci Adv 2020;6(20):eaba3884. [PubMed: 32426510]
60. Li W, Grgac K, Huang A, Yadav N, Qin Q, van Zijl PC. Quantitative theory for the longitudinal relaxation time of blood water. Magn Reson Med 2016;76(1):270–281. [PubMed: 26285144]
61. Li W, van Zijl PCM. Quantitative theory for the transverse relaxation time of blood water. NMR Biomed 2020;33(5):e4207. [PubMed: 32022362]
62. Gore JC, Brown MS, Mizumoto CT, Armitage IM. Influence of glycogen on water proton relaxation times. Magn Reson Med 1986;3(3):463–466. [PubMed: 3724426]
63. Yadav NN, Xu J, Bar-Shir A, Qin Q, Chan KW, Grgac K, Li W, McMahon MT, van Zijl PC. Natural D-glucose as a biodegradable MRI relaxation agent. Magn Reson Med 2014;72(3):823–828. [PubMed: 24975029]

64. Goldenberg JM, Pagel MD, Cardenas-Rodriguez J. Characterization of D-maltose as a T2 -exchange contrast agent for dynamic contrast-enhanced MRI. Magn Reson Med 2018;80(3):1158–1164. [PubMed: 29369407]

65. Xu X, Xu J, Chan KWY, Liu J, Liu H, Li Y, Chen L, Liu G, van Zijl PCM. GlucoCEST imaging with on-resonance variable delay multiple pulse (onVDMP) MRI. Magn Reson Med 2019;81(1):47–56. [PubMed: 30058240]

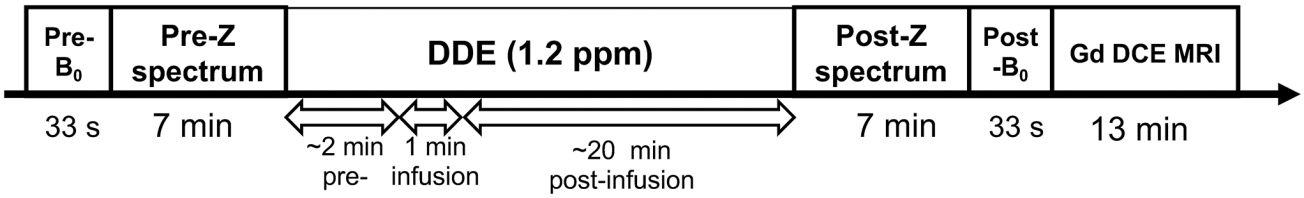

Figure 1. Timeline of CEST and DCE MRI acquisitions.

Two 7-min steady state full Z-spectra acquisitions were performed before and at approximately 10 minutes after the injection of 2 g/kg Dex1 in saline solution (infusion time=1 min). Dynamic CEST MRI was started at 2 min before the injection to 18 min after the injection at a temporal resolution of 10 s. Two WASSR scans (~ 33 sec) were acquired to assess the B_0 inhomogeneities before and after each CEST acquisition. Dynamic contrast-enhanced (DCE) MRI was acquired using a T_{1w} single-slice FLASH sequence (TR/TE=18/3 ms) from 1 min before the injection to 12 min after the i.v. injection of ProHance® (0.05 mL bolus over ~3 s).

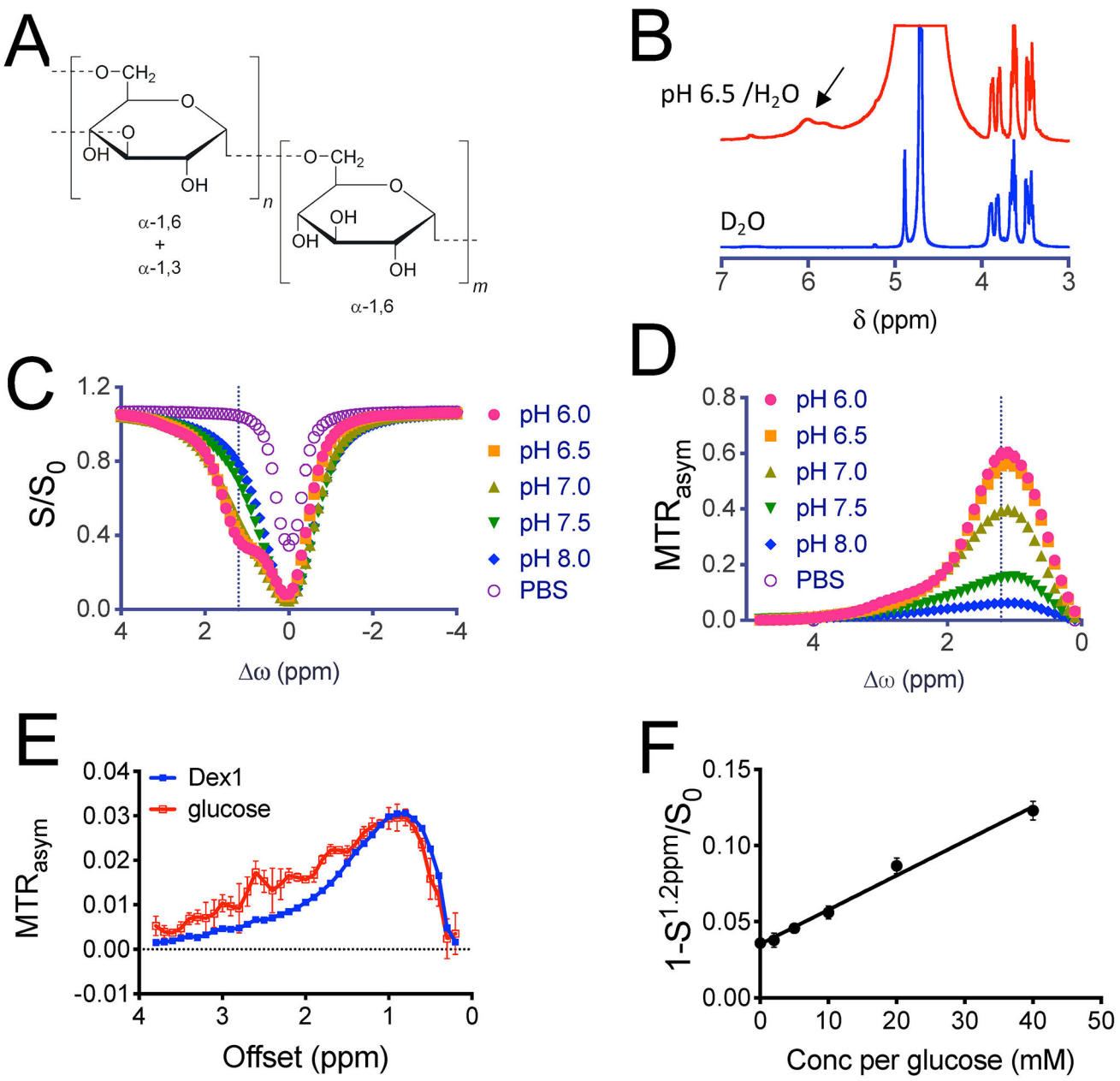

Figure 2. In vitro CEST characterization of Dex1.

a) The chemical structure of dex1 (average m = 6). **B)** NMR spectra of 100 mM dex1 in D_2O and H_2O (pH 6.5, 20 °C). **C**) Z-spectra, and **D)** MTR_{asym} plots of 20 mM Dex1 (20 mg/mL) and PBS at pH 6.0–8.0. **E)** Comparison of CEST signal of 1.8 mg/mL Dex1 (concentration per glucosyl unit ~ 22 mM) and 20 mM glucose at pH =7.4. **F)** Plot of $1\text{-}S^{1.2ppm}/S_0$ at pH = 7.4 vs. concentration of Dex1 (in glucose units), showing a good linear correlation. All studies were performed using 3-second long CW pulse (B_1 =1.8 μT) at 37°C unless otherwise noted.

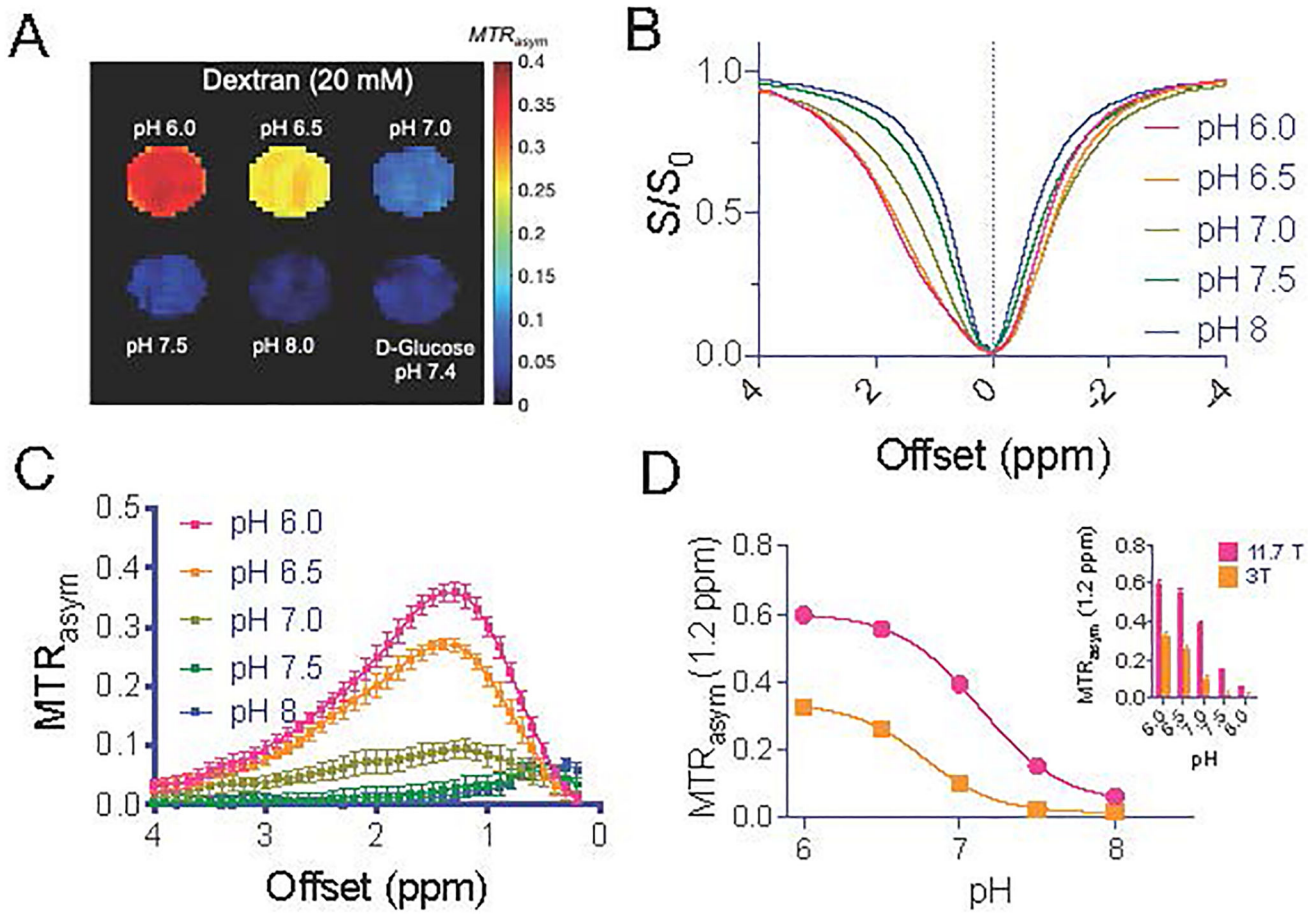

Figure 3. DexCEST (B_1=1.8 μT/3 sec) contrast at 3T.

A) MTR_{asym} parametric maps of Dex1 (20 mM) at a function of pH (37 °C). Note that a D-glucose sample (20 mg/mL, pH 7.4) was included as control. B) Z-spectra and C) MTR_{asym} of 10 mM Dex1 at pH ranging from 6.0 to 8.0. D) pH dependency of DexCEST contrast at 3T as compared to that at 11.7T.

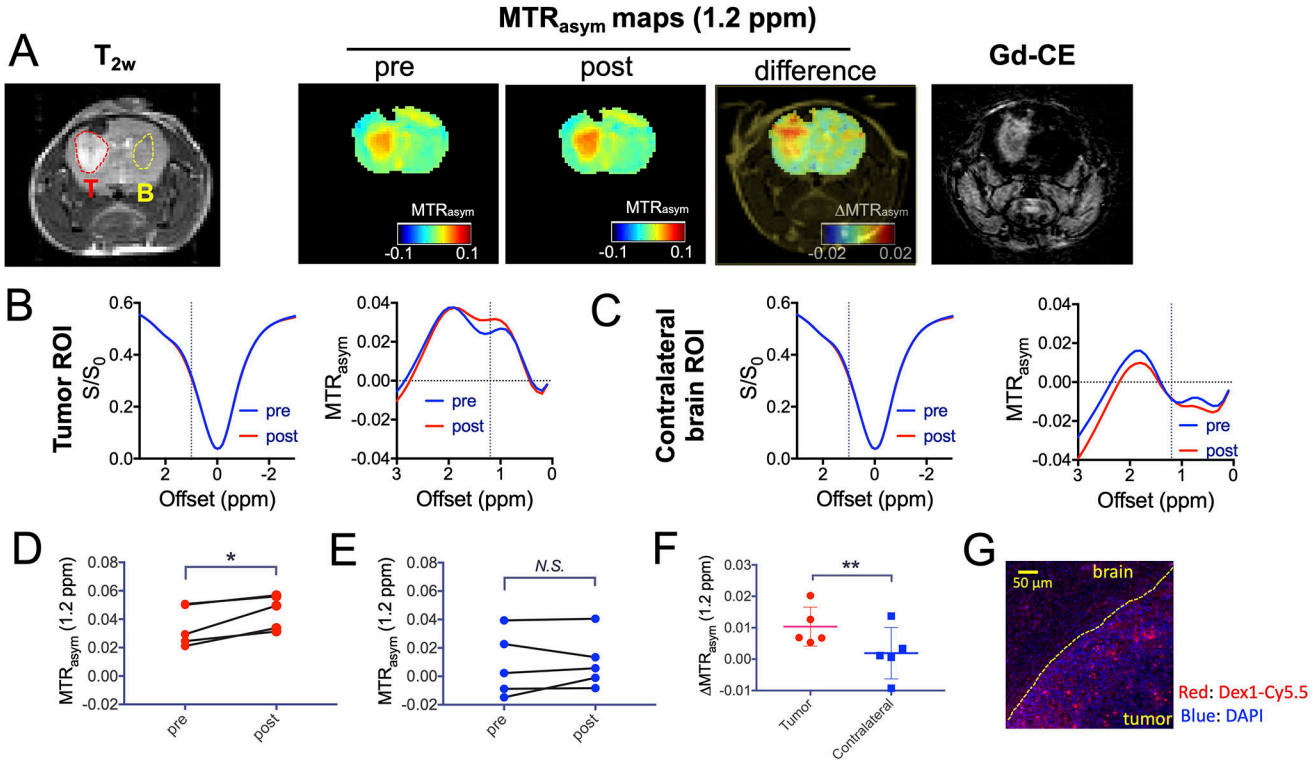

Figure 4. Dex1-enhanced CEST MRI in the GL261 brain tumor model.

A) From left to right: T2w, CEST images, and Gd-enhanced image of a representative mouse. **B**-**C**) Mean ROI Z-spectra and MTR_{asym} plots before and after dextran1 injection in the tumor (**B**) and contralateral brain (**C**). **D**-**E**) Comparison of the pre- and post-injection CEST contrast in the tumor (**D**) and brain (**E**) of 5 mice. **F**) Comparison of dextran1-induced contrast enhancement in the tumor and brain in 5 mice. **G**) Immunofluorescence image showing the high uptake of Dex1 in the tumor, in which blue is nuclei (stained with DAPI) and red is dextran (labeled with Cy5.5). Right lower area: tumor; left upper area: normal brain. *: P<0.05, **: P<0.01, *N.S.*= not significant (Student's t test, two tailed and paired, n=5).

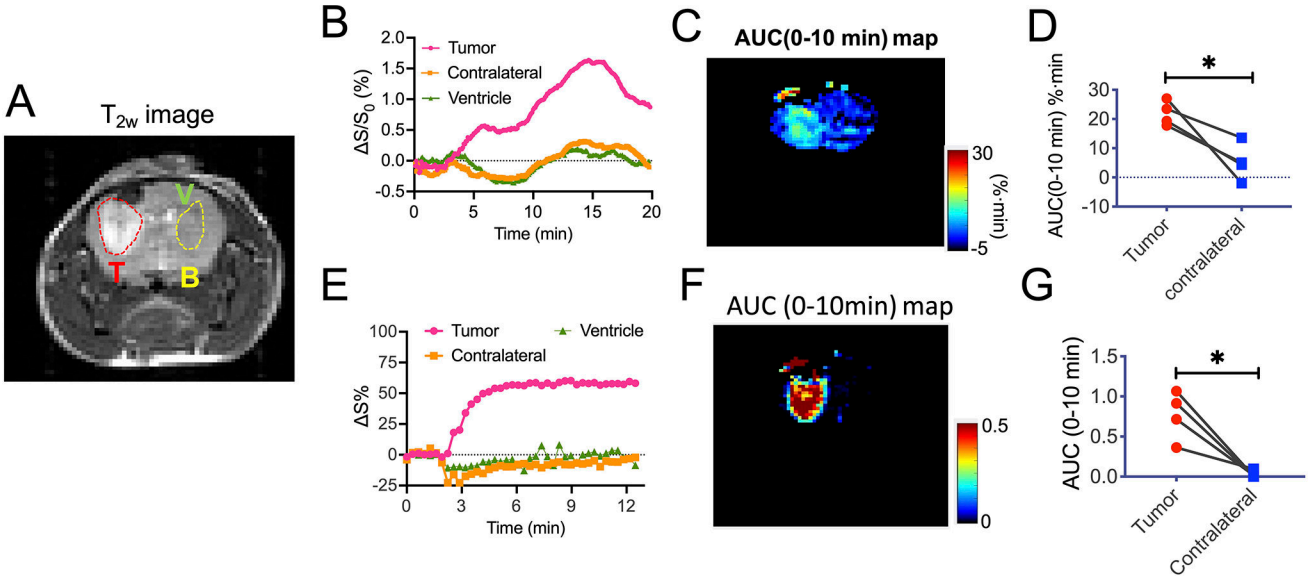

Figure 5. DDE CEST MRI in the GL261 brain tumor model.

A) T_2w image showing the three ROIs for tumor (T), brain (B) and ventricle (V). **B-D**) Dynamic changes of the mean CEST contrast, as quantified by $\Delta S^{1.2ppm}/S_0$ (t)%= $[S^{1.2ppm}/S_0$ (t=0)- $S^{1.2ppm}/S_0$ (t)]x100% (B). **C**) AUC map between 0 to 10 min after the injection of Dex1. **D**) Comparison of the mean AUC values in the tumor and brain. **E-F**) Dynamic Gd concentration change after the injection of 0.1 mmol/kg ProHance (~ 0.05 mL of 0.5 M solution). **F)** DCE AUC (0–10 min) map. **G**) Comparison of the mean AUC (0–10 min) in the tumor and brain. *: P<0.05 (Student's t test, two tailed and paired, n=4).

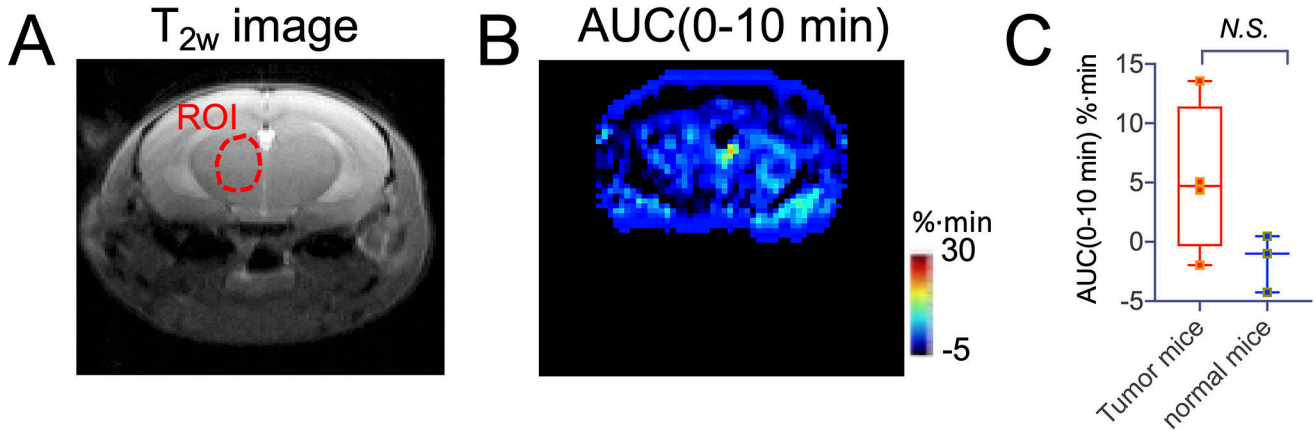

Figure 6. DDE MRI in the normal brain.

A) T_2w image of a representative mouse **B**) AUC map between 0 to 10 min after the injection of Dex1.**C**) Comparison of the mean AUC (0–10 min) in non-tumor bearing mice with that of tumor in tumor-bearing mice.